

Titre: Stability and excitation dynamics of an argon micro-scaled
Title: atmospheric pressure plasma jet

Auteurs: M. Dünnbier, M. M. Becker, S. Iseni, R. Bansemer, D. Loffhagen,
Authors: Stephan Reuter, & K. D. Weltmann

Date: 2015

Type: Article de revue / Article

Référence: Dünnbier, M., Becker, M. M., Iseni, S., Bansemer, R., Loffhagen, D., Reuter, S., &
Citation: Weltmann, K. D. (2015). Stability and excitation dynamics of an argon micro-
scaled atmospheric pressure plasma jet. Plasma Sources Science and Technology,
24 (6). <https://doi.org/10.1088/0963-0252/24/6/065018>

Document en libre accès dans PolyPublie

Open Access document in PolyPublie

URL de PolyPublie: <https://publications.polymtl.ca/4851/>
PolyPublie URL:

Version: Version officielle de l'éditeur / Published version
Révisé par les pairs / Refereed

Conditions d'utilisation: CC BY
Terms of Use:

Document publié chez l'éditeur officiel

Document issued by the official publisher

Titre de la revue: Plasma Sources Science and Technology (vol. 24, no. 6)
Journal Title:

Maison d'édition: IOP Publishing
Publisher:

URL officiel: <https://doi.org/10.1088/0963-0252/24/6/065018>
Official URL:

Mention légale:
Legal notice:

PAPER • OPEN ACCESS

Stability and excitation dynamics of an argon micro-scaled atmospheric pressure plasma jet

To cite this article: M Dünnbier *et al* 2015 *Plasma Sources Sci. Technol.* **24** 065018

View the [article online](#) for updates and enhancements.

Related content

- [Spatio-temporal plasma heating mechanisms in a radio frequency electrothermal microthruster](#)
Scott J Doyle, Andrew R Gibson, Jason Flatt *et al.*
- [Mechanisms of sustaining a radio-frequency atmospheric pressure planar discharge](#)
Lei Wang, Gheorghe Dinescu, Xiaolong Deng *et al.*
- [Analysis of microdischarges in asymmetric dielectric barrier discharges in argon](#)
M M Becker, T Hoder, R Brandenburg *et al.*

Recent citations

- [Comparison of electron heating and energy loss mechanisms in an RF plasma jet operated in argon and helium](#)
J Golda *et al*
- [Control of electron dynamics, radical and metastable species generation in atmospheric pressure RF plasma jets by Voltage Waveform Tailoring](#)
I Korolov *et al*
- [On a non-thermal atmospheric pressure plasma jet used for the deposition of silicon-organic films](#)
Jan Schäfer *et al*



IOP | ebooks™

Bringing you innovative digital publishing with leading voices to create your essential collection of books in STEM research.

Start exploring the collection - download the first chapter of every title for free.

Stability and excitation dynamics of an argon micro-scaled atmospheric pressure plasma jet

M Dünnbier^{1,2}, M M Becker¹, S Iseni^{1,2,3}, R Bansemer^{1,2}, D Loffhagen¹, S Reuter^{1,2} and K-D Weltmann¹

¹ Leibniz Institute for Plasma Science and Technology e.V. (INP Greifswald), Felix-Hausdorff-Str. 2, 17489 Greifswald, Germany

² Centre for Innovation Competence Plasmatis, Felix-Hausdorff-Str. 2, 17489 Greifswald, Germany

E-mail: stephan.reuter@inp-greifswald.de

Received 1 July 2015, revised 18 September 2015

Accepted for publication 30 September 2015

Published 17 November 2015



Abstract

A megahertz-driven plasma jet at atmospheric pressure—the so-called micro-scaled atmospheric pressure plasma jet (μ APPJ)—operating in pure argon has been investigated experimentally and by numerical modelling. To ignite the discharge in argon within the jet geometry, a self-made plasma tuning unit was designed, which additionally enables measurements of the dissipated power in the plasma itself. Discharges in the α -mode up to their transition to the γ -mode were studied experimentally for varying frequencies. It was found that the voltage at the α - γ transition behaves inversely proportional to the applied frequency f and that the corresponding power scales with an $f^{3/2}$ law. Both these findings agree well with the results of time-dependent, spatially one-dimensional fluid modelling of the discharge behaviour, where the $f^{3/2}$ scaling of the α - γ transition power is additionally verified by the established concept of a critical plasma density for sheath breakdown. Furthermore, phase resolved spectroscopy of the optical emission at 750.39 nm as well as at 810.37 nm and 811.53 nm was applied to analyse the excitation dynamics of the discharge at 27 MHz for different applied powers. The increase of the power leads to an additional maximum in the excitation structure of the 750.39 nm line emission at the α - γ transition point, whereas the emission structure around 811 nm does not change qualitatively. According to the fluid modelling results, this differing behaviour originates from the different population mechanisms of the corresponding energy levels of argon.

Keywords: argon atmospheric pressure plasma jet, dissipated power, experiment and modelling, α - γ -mode transition, excitation dynamics

(Some figures may appear in colour only in the online journal)

1. Introduction

Atmospheric pressure plasma jets have garnered increasing interest in the past decade due to their applicability in research fields such as plasma medicine, involving various biomedical

applications ranging from surface modification and biological decontamination to therapeutic treatment [1, 2]. Plasma jets have several advantages compared to volume or surface dielectric barrier discharges particularly concerning the enhanced control of discharge conditions and reactive species output. However, a feed gas has to be supplied for the operability of plasma jets. Commonly noble gases are used for this purpose.



Content from this work may be used under the terms of the [Creative Commons Attribution 3.0 licence](https://creativecommons.org/licenses/by/3.0/). Any

further distribution of this work must maintain attribution to the author(s) and the title of the work, journal citation and DOI.

³ Current address: GREMI, UMR 7344, CNRS/Université d'Orléans, BP 6744, 45067 Orléans Cedex 2, France

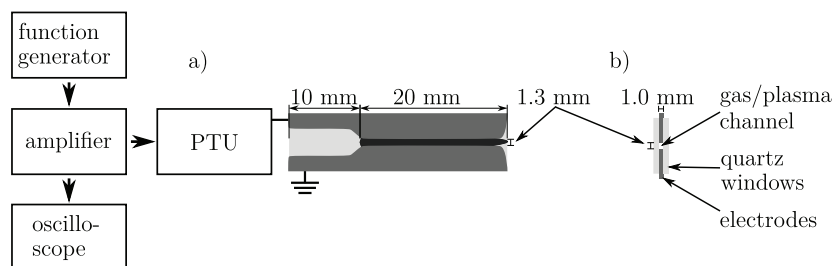


Figure 1. Schematic of the argon micro-scaled atmospheric pressure plasma jet and the power supply including the function generator, amplifier, oscilloscope and plasma tuning unit (PTU) with (a) side view and (b) front view.

The feed gas strongly affects the electron energy distribution function and consequently the production of the biologically active reactive species.

The micro-scaled atmospheric pressure plasma jet (μ APPJ) was developed to get an optimal optical access to the discharge region [3–6]. Furthermore, its simple capacitive plane-parallel electrode configuration allows simple [7] but also complex [8] modelling approaches of the plasma. For these reasons, the μ APPJ is proposed as a standard reference source for cold atmospheric pressure plasma jets as they are used in plasma medicine. Research up to now has dealt with extensive studies on the plasma conditions and dynamics [9, 10] as well as reactive species output for the jet operated in helium with small molecular gas admixtures [11, 12] or admixtures of argon [13]. Furthermore, this plasma jet fed with helium has been applied in plasma medicine (see e.g. [14]). However, the determination of the dissipated power of the plasma has proven difficult to achieve [15].

To avoid the use of the precious resource helium as the feed gas and to obtain a thorough understanding of the discharge behaviour, a modified μ APPJ working with argon has been developed and characterized. Furthermore, a concept of accurate power determination is represented and has been used for the analysis of the plasma jet. In accordance with the conventional helium μ APPJ, the plasma generated by the argon jet studied in the present work is an atmospheric pressure RF glow discharge which can be operated in two different modes: The first one is the so-called α -mode, where bulk electrons are responsible for most electron collision processes. The second mode is the γ -mode, where secondary electrons largely contribute to the ionization budget [16, 17]. In the γ -mode discharge constriction, gas heating and the development of an arc plasma occur, if the current density is not restricted appropriately [18, 19]. The transition from the α - to the γ -mode at atmospheric pressure is the result of a sheath breakdown in front of the electrodes at a certain critical power, similar to the α - γ -mode transition at low and moderate pressures [20, 21]. Thus, the α -mode can be maintained only over a limited power range. In a large scale APPJ, a comparison of argon and helium discharge showed similar behaviour [6].

Because the α -mode provides discharge conditions preferable over the γ -mode for practical applications such as low gas temperature [17], possibilities of an expansion of the α -mode stability have been investigated in recent years. Park *et al* [22] and Kong with co-workers [23–25] have found for atmospheric pressure RF glow discharge plasmas in helium that the critical power density at which a transition to the γ -mode occurs can

be increased by increasing the applied frequency. The same effect has been observed by Chirokov *et al* [19] for a helium atmospheric pressure plasma jet and by Zhang *et al* [26] for an argon atmospheric pressure RF glow discharge. Detailed investigations of the described phenomena have been performed by plasma models for different gases and discharge configurations [27, 28]. A rise of the applied frequency leads to a decrease of the oscillation amplitude of the electrons and, thus, the loss of electrons to the wall is reduced [29]. Therefore, the contribution of secondary electron emission to the ionization budget becomes increasingly unlikely compared to electron impact processes in the bulk plasma at higher frequencies.

In the present work, the α -mode stability range of the argon jet with respect to the dissipated power and the applied frequency is analysed by measurements and numerical model calculations. An explicit relation between the frequency and the α - γ -mode transition point is derived based on the measured and calculated data. In addition, the excitation dynamics within the α -mode as well as at the transition point to the γ -mode are studied. The excitation processes leading to the observed emission pattern at different input powers are identified and compared with results of time-dependent, spatially one-dimensional fluid model calculations of the argon plasma.

The manuscript is organized as follows. In section 2 the modified argon μ APPJ is introduced and its power supply is briefly described. The diagnostic approaches used for electrical and optical measurements are presented in section 3. In particular, the experimental way of determining the dissipated power of the plasma is detailed here. Section 4 gives a brief introduction of the fluid model applied for the spatio-temporal characterization of the plasma source. Experimental and theoretical results are discussed in section 5 and the paper is summarized in section 6.

2. Experimental setup of the plasma jet and the power supply

The μ APPJ used in this work has a geometry similar to the known helium μ APPJs in the literature [9]. A schematic picture of the plasma jet and its power supply is shown in figure 1. The plasma jet consists of two parallel stainless steel electrodes with a thickness of 1.0 mm covered with quartz glass windows from both sides. Compared to the reference plasma jet, the gap between the electrodes is enlarged to 1.3 mm and the length of the discharge channel is shortened to 20.0 mm. Consequently, the embedded discharge channel

has a volume of $V = 26 \text{ mm}^3$ which is similar to the standard μAPPJ with 30 mm^3 [9]. The larger discharge gap reduces the ratio of electrons lost to the wall to the electron multiplication in the bulk and thus extends the stability range of the α -mode.

The power is supplied by means of a function generator (AFG3252, Tektronix), which generates a sinusoidal RF voltage waveform. The present experiment uses a symmetrical bipolar periodical sinusoidal waveform in the range from 13 to 36 MHz. The output of the function generator is connected to the amplifier input (SCCX100, Instruments For Industry). The power dissipated in the plasma is measured by means of an oscilloscope (DPO4104, Tektronix) mounted to the sample ports of the amplifier. Details of the dissipated power measurement are given in section 3.1.

To dissipate the maximum power into the plasma, the impedance of the power supply (50Ω) and the plasma jet have to be matched. The impedance of the plasma $Z_{\text{Pl}} = R_{\text{Pl}} + iX_{\text{Pl}}$ with the plasma resistance R_{Pl} , $i = \sqrt{-1}$ and the plasma reactance X_{Pl} is mainly affected by the capacitive reactance ($X_{\text{Pl,C}} = -1/(\omega C_{\text{Pl}})$) due to the geometry of two parallel electrodes. This capacitive character of the plasma is matched by a plasma tuning unit (PTU) consisting of a coil located directly in front of the plasma jet. The cylindrical coil has a reactance $X_{\text{PTU}} = \omega L$ with the inductance L and angular frequency $\omega = 2\pi f$. The best matching is achieved when the reactance of the plasma and the PTU are similar. This is achieved in two steps. Firstly, a proper inductance of the coil is chosen. Secondly, the reactance X_{PTU} is tuned by slightly changing the applied frequency in a way that the reflection coefficient is minimized for the case when a discharge is ignited between the electrodes of the plasma jet. The reflection coefficient is defined as the ratio of the reflected power $P_{\text{back,on}}$ to the forward power $P_{\text{for,on}}$. The PTU is installed between the output of the amplifier and the powered electrode of the plasma jet using N-type RF connectors. The other jet-electrode is grounded. A small visible effluent in front of the jet is created when the voltage is applied and the feed gas of $\Phi = 1 \text{ slm}$ argon is piped into the discharge region of the jet. The jet is mounted without the use of glue near the plasma channel to prevent an influence of the glue on the discharge.

3. Experimental diagnostics

In the following, the diagnostic approaches and experimental setups implemented for the investigation of the plasma source are presented. Firstly, the electrical characterization of the plasma device is performed in order to gain access to the values of the dissipated power into the plasma. Secondly, phase resolved optical emission spectroscopy is applied to analyse the spatio-temporal behaviour of selected argon emission lines in correlation with the electrical excitation dynamics.

3.1. Electrical characterization and dissipated power measurement

Dissipated power determination of atmospheric pressure RF plasma jets is a difficult matter due to the small dimensions

of the jets resulting in a small impedance and capacitance. Established techniques are limited by the applied frequency of the plasma jet and the resulting wave nature of the physical values. Due to the frequency range used for the plasma jet under investigation, the dissipated power determination has to be adapted based on techniques introduced in the literature. Firstly, the established methods are explained briefly in this section and secondly, the modified power measurement arrangement is introduced.

Electrical information is often required to monitor a plasma and influence its properties. Generally, the average power of an electric signal of period $T = 1/f$ is defined by

$$P = \frac{1}{T} \int_{t_0}^{t_0+T} I(t) \cdot V(t) dt \quad (1)$$

with $I(t)$ and $V(t)$ being the instantaneous current and voltage, respectively, at a given time t and point in the electrical circuit. In case of a sinusoidal waveform, equation (1) can be written as

$$P = I_{\text{RMS}} \cdot V_{\text{RMS}} \cdot \cos(\phi) \quad (2)$$

where $I_{\text{RMS}} = I_0/\sqrt{2}$ and $V_{\text{RMS}} = V_0/\sqrt{2}$ are the root mean square (RMS) current and voltage, respectively. Both quantities are related to each other by the phase ϕ . Usually, the total power delivered by the generator into the electrical network down to the plasma can be determined from measurements of current, voltage and phase directly at the electrodes. Unfortunately, the present combination of RF waveforms and resonant circuit is sensitive to diagnose, mostly because the resistance as well as the reactance of the voltage probe are in the same order of magnitude as the respective values of the jet and the coil. In the present work, the capacitance of the plasma jet is about 2 pF and the capacitance of the voltage probe is 8 pF (Tektronix P6139A 10X). Therefore, it is difficult to distinguish the portion of power dissipated in the jet from the portion dissipated in the probe. Additionally, the capacitance of the probe influences the matching between the coil and the jet. This fact was reported by Hofmann *et al* [30] for the power measurement of a similar atmospheric pressure plasma jet.

Other RF power measurement possibilities involving capacitive and inductive probes have been applied, requiring a full complex impedance characterization of the probes as shown in [31]. Nevertheless, recently Marinov *et al* [15] succeeded in measuring the power dissipated into a helium plasma ignited in a similar apparatus geometry by means of a commercially calibrated standalone electrical probe based on the approach reported by [31].

According to Godyak *et al* [32] and Hofmann *et al* [30], the voltage and current probes have to be placed between the generator and the matching coil. This implies that the dissipated power is measured for the system consisting of coil and plasma jet. In this case, the power dissipated into the plasma P_{dis} can be deduced from

$$P_{\text{dis}}(I_{\text{RMS}}) = P_{\text{on}}(I_{\text{RMS}}) - P_{\text{off}}(I_{\text{RMS}}), \quad (3)$$

where P_{on} and P_{off} denotes the dissipated power for the on- and the off-case of the plasma, respectively. This subtraction

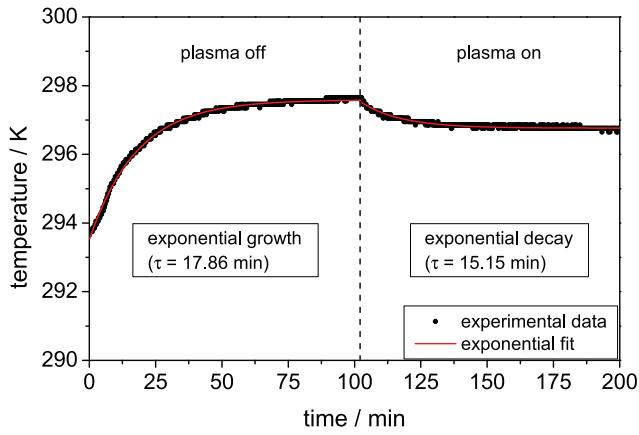


Figure 2. Temporal evolution of the temperature inside the PTU for the plasma off and on case. The system was switched on at $t = 0$ min and the plasma at $t = 110$ min.

method has been successfully used under the main assumption that the power consumed by the coil has to be constant independent of the plasma on or off state. Indeed, the losses caused by the coil are from its resistive feature and result in Joule heating. To validate this assumption, the temporal evolution of the temperature of the coil used for the plasma jet under investigation is recorded for both conditions as depicted in figure 2. It is found that the temperature of the coil increases slightly by 4 K while the system is powered without plasma and reaches a steady state after 90 min corresponding approximately to five times the exponential rise time 17.86 min. The turning-on of the plasma leads to a slight decrease by about 0.8 K with an exponential decay time of about 15.15 min. Thus, it does not significantly affect the coil temperature and the power loss can be assumed constant with or without plasma. The minor change corresponding to $\Delta T_{\text{coil}} = 0.8$ K is within the instrumental accuracy of the temperature sensor (FOTEMP1-OEM, Optocon). It has to be noted that it can also be due to a better impedance matching once the plasma is turned on. However, it becomes obvious that the PTU needs around two hours until it reaches the stationary regime. Therefore, before starting a measurement the system was switched on 2 h in advance.

Thus, sampling the current and voltage in the position between the generator and the matching coil could be realized as in [30]. However, as mentioned in section 2 the symmetric sinusoidal frequency used for the plasma jet under investigation is in the order of 10–40 MHz. As a consequence the wavelength of the applied voltage inside a coaxial cable with a permittivity of about 2.3 is in the range between 5 and 20 m, which is in the order of magnitude of the used cable length (1 m). Because of the wave nature of the applied voltage with located minima and maxima, the current and voltage values are dependent on the location of the measurement point in the cable. Therefore, special care has to be taken when determining the dissipated power. Furthermore, one has to distinguish between the forward and backward direction of the voltage and current values. Applying error propagation on the power value yields an error of about 90% when assuming a reasonable measurement deviation of 1% for each quantity of equation (2). Due to the relatively low power applied to

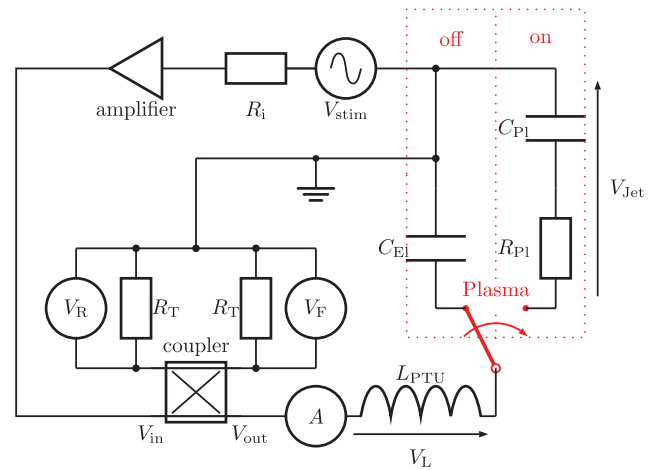


Figure 3. Resonant circuit of the experimental setup with the power supply (V_{stim}) with $R_i = 50 \Omega$, the directional coupler, the voltage probes (V_R , V_F) connected to the sample ports with $R_T = 50 \Omega$, the plasma tuning unit (L_{PTU}) and the plasma jet for the plasma on and off case. C_{El} refers to the electrical capacitance without plasma and R_{Pl} and C_{Pl} denote the resistance and capacitance for the plasma on case, respectively. The current probe (A) is placed directly in front of the coil. V_{in} and V_{out} are the RMS voltages belonging to the wave travelling inside the coupler input and away from the coupler output. V_L corresponds to the voltage drop over the coil and V_{Jet} to the voltage drop over the plasma jet.

this plasma jet, such uncertainty can often result in a negative calculated dissipated power.

In order to overcome these difficulties, the methods discussed in the literature have to be adapted. Therefore, a different electrical sampling approach involving a directional coupler has been implemented in the power measurement of high RF powered micro-scaled plasma jet. The calibration of the directional coupler and the corresponding coupling factors (k_R , k_F) were characterized beforehand with test signals produced by a function generator (AFG3252, Tektronix) and measured with an oscilloscope (DPO4104, Tektronix). Therefore, the ratio of the voltage signals of $V_{\text{out},F}/V_F$ and $V_{\text{out},R}/V_R$ were measured as a function of the applied frequency as depicted in figure 3. $V_{\text{out},F}$ and $V_{\text{out},R}$ are the RMS voltages belonging to the wave travelling away from the coupler output (forward) and into the coupler output (reflected) and V_F and V_R denote the forward and reflected voltage measured by the probes. These coupling factors describe the ratios of the voltage values of the signal port to the sample ports. The same oscilloscope as for the calibration procedure is used to measure the power which is dissipated in the plasma off and on case given by

$$P_{\text{off}} = \frac{V_{F,\text{off}}^2 \cdot k_F^2 - V_{R,\text{off}}^2 \cdot k_R^2}{R_T} \quad (4)$$

$$P_{\text{on}} = \frac{V_{F,\text{on}}^2 \cdot k_F^2 - V_{R,\text{on}}^2 \cdot k_R^2}{R_T} \quad (5)$$

by determining V_F and V_R for both situations with $R_T = 50 \Omega$. The measurement of the reflected voltage V_R is necessary because the matching between the PTU and the plasma is not perfect. Then, the power P_{dis} dissipated in the plasma is

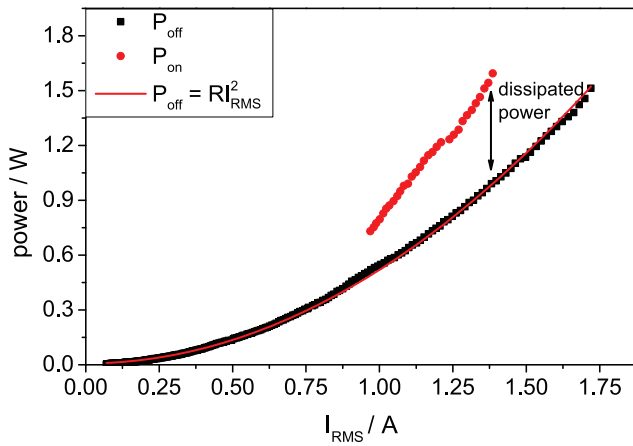


Figure 4. Power as a function of the RMS current I_{RMS} for the plasma on and off case at a frequency of 27 MHz.

Table 1. Inductance of the coils used for the different applied frequencies.

Frequency / MHz	Inductance / μH
13.1	10.7
20.4	4.3
36.1	1.4

determined according to equation (3) by subtracting P_{off} from P_{on} . The error of the dissipated power is calculated considering the propagation of uncertainties including the error of 1% for each quantity of equation (4) and (5) resulting in an error of the dissipated power of about 10%.

An illustration of the plasma deposited power determination as a function of the current is presented in figure 4. The current is measured with a current probe (CT1, Tektronix) between the generator and the PTU, see figure 3. The measurements show that the losses caused by the coil are well described by $P_{\text{off}} \propto I_{\text{RMS}}^2$ in accordance with Joule's law, which consolidates the applicability of the method.

As described above, the electrode voltage cannot be measured directly at the electrodes for the given plasma jet and conditions. Therefore, the trend of the voltage at the electrode is evaluable using the current probe as shown in figure 3. For a sinusoidal current waveform the inductance of the coil, the frequency and the RMS current can be used to calculate the RMS voltage drop over the coil according to

$$V_{\text{L,RMS}} = I_{\text{RMS}} \cdot 2\pi f \cdot L. \quad (6)$$

The change of the operation voltage V_{out} leads to a change in both of its components V_{L} and V_{jet} . The ratio between both components remains constant, because their impedance ratio can be assumed to be fixed. Therefore, the slope of the voltage V_{L} is the same as the slope of the voltage at the electrodes of the jet V_{jet} . Consequently, only relative voltage values are compared to modelling results in section 5.

The inductance of the different coils inside the PTU are listed in table 1. Notice that for the PROES measurement at a frequency of 27 MHz no voltage determination was possible. The error of the RMS voltage at the electrodes

is calculated considering the propagation of uncertainties including the error of the inductance determination ($0.1 \mu\text{H}$) and the accuracy of the current measurements (3%). It amounts to about 20%.

3.2. Phase resolved optical emission spectroscopy

Phase resolved optical emission spectroscopy (PROES) is a powerful non-invasive diagnostic tool to gain information on the spatial and in particular the temporal development of the emission of excited species [33]. In order to measure the emission of the excited species, a high-repetition rate gated intensified charge-coupled device (iCCD) camera (PicoStar HR12, LaVision) has been used with a spatial resolution of $8 \mu\text{m}$. The experimental setup and the procedure of the PROES measurements are shown in figure 5.

The basic principle of PROES is that a gated iCCD image is acquired at a certain instant within the RF period. The gate width is typically 1–10% of one RF excitation cycle [34] and in the present case the time is fixed to 500 ps. One image is averaged over several thousands of RF cycles. Then, the image acquisition starting time is shifted by about one gate width using a delay generator. This method allows one to record a space- and time-dependent map of the excited species correlated to the electric excitation frequency.

In order to measure the emission of the selected excited argon species $\text{Ar}(2p_1)$, $\text{Ar}(2p_7)$ and $\text{Ar}(2p_9)$ (Paschen notation), see figure 6, two filters ($\lambda_{\text{C}} = 750.495 \text{ nm}$ with $\lambda_{\text{FWHM}} = 0.352 \text{ nm}$ and $\lambda_{\text{C}} = 811.00 \text{ nm}$ with $\lambda_{\text{FWHM}} = 7.25 \text{ nm}$), respectively, were used in front of the PROES system. These three lines can be associated with electron impact excitation. In particular, it was found for the measurements at 27 MHz discussed below that the emission intensity of the $\text{Ar}(2p_7)$ at 810.37 nm is about 20% of the emission intensity of the $\text{Ar}(2p_9)$ line at 811.53 nm . Optical emission spectroscopy measurements of the discharge (not shown here) indicate that only the discussed lines are detected in the PROES setup and no significant background was measured.

4. Numerical model

In order to support the experimental investigations of the atmospheric pressure plasma jet, the time-dependent, spatially one-dimensional fluid-Poisson model described in detail in [36] was adapted for numerical modelling of the argon plasma under consideration. The mathematical model includes balance equations for the densities of electrons, atomic and molecular argon ions as well as seven excited atomic and four excited molecular neutral argon species. Additionally, a balance equation for the mean electron energy density and Poisson's equation for determination of the electric field are included. Regarding the seven excited atomic argon species, the implemented reaction kinetic model includes the energy levels $1s_5$ – $1s_2$ listed in figure 6. For higher levels the lumped states $2p$ (including $2p_{10}$ – $2p_5$), $2p'$ (including $2p_4$ – $2p_1$) and hl (including all higher lying states) are introduced in [36].

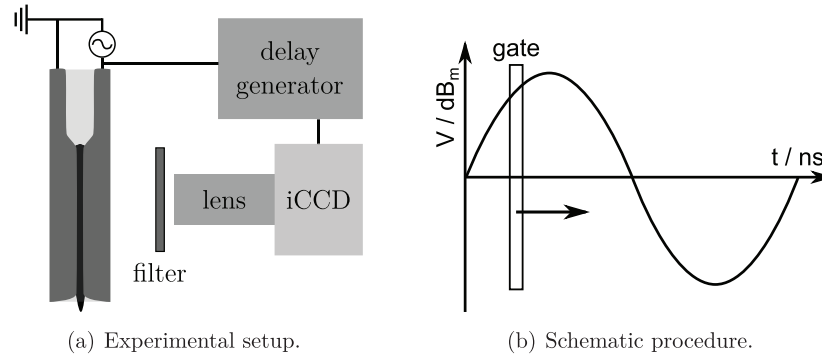


Figure 5. (a) Experimental setup of the PROES measurements. The filter is used in order to quantify the phase resolved emission of a selected line. (b) Schematic procedure for the PROES measurements depicted on one excitation RF cycle. The gate is open for 500 ps and then moved to the next point in time until the end of the cycle is reached.

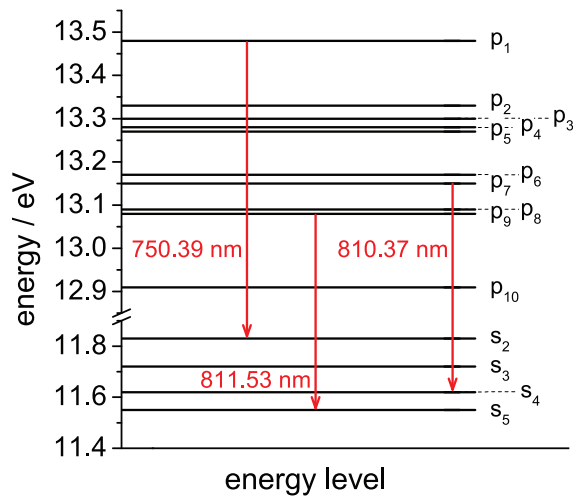


Figure 6. Transition of the obtained argon lines with the corresponding energy levels [35]. The three lines indicated with red arrows are investigated within this study.

The electron energy balance equation including an improved drift-diffusion approximation [37, 38] for the electron particle and energy fluxes is taken into account to describe adequately the spatio-temporal transport of electron energy. The transport and rate coefficients of the electrons are determined in advance from the solution of the steady-state, spatially homogeneous electron Boltzmann equation using the same collision cross section data as in [36]. The kinetic equation of the electrons has been solved for given electric field, gas temperature, pressure and cross section data in multiterm approximation of the expansion of the electron velocity distribution function in Legendre polynomials using a generalized version of the method described in [39]. It has been adapted to take nonconservative electron collisions and the random motion of gas particles into account. The resulting transport and rate coefficients of the electrons have subsequently been put into look-up tables as a function of the mean electron energy. These mean-energy-dependent coefficients are then used in the fluid model calculations. This common approach, see e.g. [40], is also known as local-mean-energy approximation [41].

The reaction kinetic model includes 115 processes. In addition to elastic electron-argon collisions involved in the

balance equation for the mean electron energy density, about 80 inelastic collision processes contribute to the balance equations of the electrons. These processes comprise electron impact excitation, de-excitation and ionization and electron-ion recombination with rate coefficients depending on the mean electron energy as well as chemo-ionization processes. Furthermore, a charge-transfer reaction as well as quenching and radiative processes of excited argon species are taken into account with respect to the heavy particle kinetics.

The considered model allows the prediction of the spatio-temporal plasma behaviour between the electrodes separated by a gap $d = 1.3$ mm. Details of the boundary conditions at the electrodes are given in [36]. In the framework of the spatially one-dimensional description (in the x -direction), it is assumed that the gas flow along the jet axis does not influence the basic plasma properties significantly and that the influence of plasma gradients in transverse direction is negligible. To validate this approach, the residence time

$$\tau = \frac{V}{\Phi} \frac{T_0}{T_{\text{gas}}} \quad (7)$$

of gas particles in the active plasma volume is determined, where $T_0 = 273.15$ K denotes the gas temperature at standard conditions. From this equation, residence times in the order of one second are obtained as long as the gas temperature T_{gas} does not increase significantly. Therefore, characteristic time scales inherent in the discharge plasma are much shorter than the residence time and thus the gas flow can safely be neglected.

Starting from a spatially homogeneous, quasi-neutral state with heavy particle densities of 10^6 cm^{-3} , an electron density of $2 \times 10^6 \text{ cm}^{-3}$ and a mean electron energy of 1.5 eV, the temporal evolution of the plasma is traced until it reaches a periodic state. Note that the final periodic state is not influenced by the specific initial values chosen. All calculations were carried out for the specified experimental conditions assuming a constant gas temperature of 350 K. This value was chosen in accordance with an experimental estimation of the gas temperature by means of line broadening measurements in [42].

In order to be able to compare the modelling results directly to the measured data and to investigate the α - γ -mode

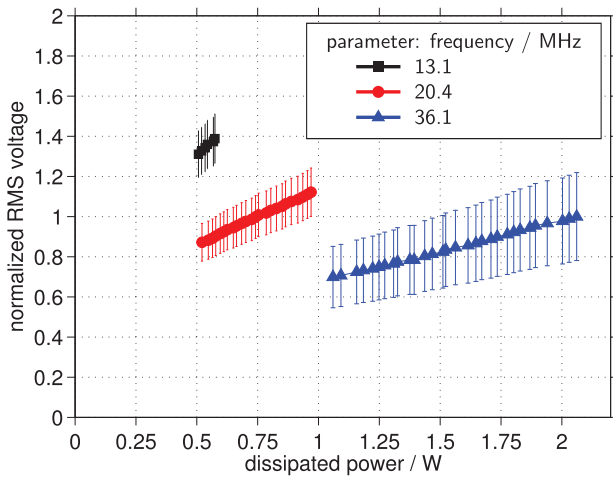


Figure 7. Measured RMS voltage of the plasma jet as a function of the dissipated power for three different frequencies. All voltages values are normalized to the maximal voltage at 36.1 MHz.

transition, the measured dissipated power was used as input for the numerical calculations. Therefore, the voltage V_0 applied to the powered electrode was automatically adapted in each period according to [7]

$$V_0^{\text{new}} = V_0^{\text{old}} \left(\frac{P_{\text{exp}}}{P_{\text{calc}}} \right)^c, \quad 0 < c \leq 1 \quad (8)$$

until reaching the periodic state. Here, P_{exp} and P_{calc} are the measured and the actual averaged calculated power, respectively, and $c = 0.25$ has been used. This procedure ensures that $P_{\text{calc}} = P_{\text{exp}}$ when the periodic state is reached. In the model, at each instant t_0 the dissipated power was calculated by the expression

$$P_{\text{calc}}(t_0) = \frac{A_{\text{dis}}}{T} \int_{t_0}^{t_0+T} \int_0^d J_{\text{ch}}(x, t) E(x, t) dx dt \quad (9)$$

with the total charge carrier flux J_{ch} and the electric field E . It was assumed that the plasma covers uniformly the complete cross-sectional area $A_{\text{dis}} = 20 \text{ mm}^2$ of the jet (see figure 1).

5. Results and discussion

Experimental and numerical results of the electrical characteristics of the modified argon μ APPJ and its excitation dynamics are presented and discussed within the following sections.

5.1. Electrical characteristics and α to γ mode transition

In figure 7 the measured change of the RMS voltage with changing dissipated power is shown for the frequencies specified in table 1. All values are normalized to the maximum voltage at 36.1 MHz. Note that measurements of the voltage at 27 MHz were not possible because the frequency values are fixed due to the experimental setup and the coil used in the PTU.

The normalized RMS voltages increase almost linearly with increasing dissipated power for each frequency until

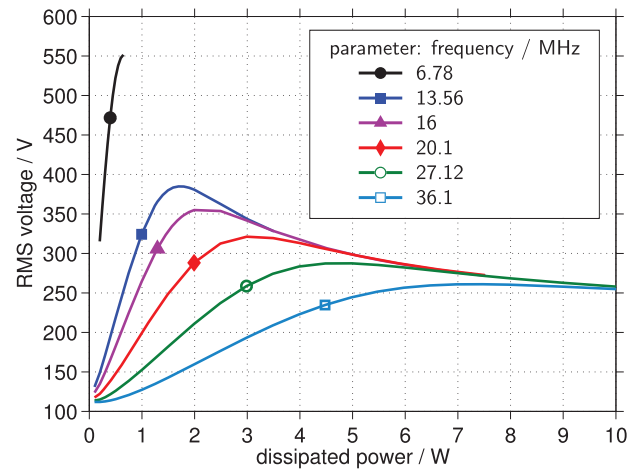


Figure 8. Calculated RMS voltage as a function of the dissipated power and α - γ transition point labelled by symbols for different frequencies.

at a critical power P_{crit} a transition to the γ -mode occurs. To prevent destruction of the plasma jet due to the higher local gas temperature in the γ -mode, at this point the power is immediately switched off. The voltage at which a transition to the γ -mode occurs decreases with increasing frequency, but at the same time the critical power P_{crit} is larger at higher frequency. This general trend is in agreement with the findings for atmospheric pressure RF glow discharge plasmas in helium and argon [25, 26]. It can be attributed to the decrease of the electron oscillation amplitude and the resulting reduction of bulk electron loss to the electrodes with increasing frequency [23, 29].

In accordance with the findings by other authors for helium-based atmospheric pressure plasma jets (see e.g. [19, 43]), the power range at which the present argon μ APPJ runs in the stable α -mode is much narrower for frequencies below 20 MHz. This is also in agreement with the theoretical results reported by Farouk *et al* [44] which show a fast α - γ transition in atmospheric pressure argon at 13.56 MHz and the results of the present fluid model calculations represented in figure 8. The change of the RMS voltage with changing power and applied frequency predicted by the present fluid modelling is in excellent qualitative agreement with the experimental results shown in figure 7.

In addition to the experimental investigation of the α -mode, the model provides the possibility of studying the electrical characteristics of the α - γ transition to some extent. However, one has to keep in mind that the transition to the γ -mode goes along with a constriction of the plasma [26] and significant gas heating [44], i.e. two effects that are not included in the model. In [44] a gas temperature rise of 200 K, mainly due to elastic electron collisions, has been reported for a comparable atmospheric pressure argon plasma. Nevertheless, the present modelling results exhibit the expected drop of the RMS voltage and a negative differential conductivity after transition to the γ -mode in figure 8.

To be consistent with the experimental data, the critical α - γ transition power P_{crit} marked in figure 8 by symbols was

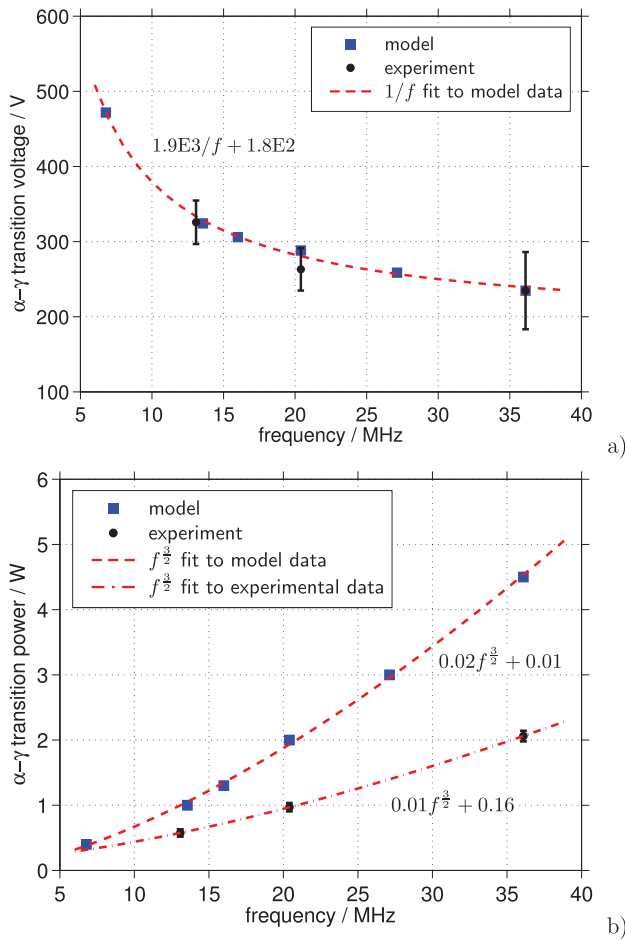


Figure 9. RMS voltage at the α - γ transition point (a) and α - γ transition power P_{crit} (b) obtained by modelling and experiment as a function of the applied frequency. Measured relative voltages are multiplied by the theoretical value at 36 MHz.

fixed at the value, at which the calculated current–voltage characteristics become nonlinear. By increasing the frequency from 13 to 36 MHz the α - γ transition power is raised by a factor of 4.5 which is about 30% larger than the factor of 3.5 of the increase of the measured transition power.

A direct comparison of the measured and the calculated RMS voltages and power values at the α - γ transition point as a function of the applied frequency is given in figure 9. Both the measured and the calculated α - γ transition voltages vary according to $1/f$ as shown in figure 9(a). When normalizing the measured RMS voltages shown in figure 7 to the modelling result at 36 MHz, good agreement between the measured and calculated absolute values is found for the entire frequency range.

For the α - γ transition power represented in figure 9(b) as a function of the applied frequency f the scaling law $P_{\text{crit}} \sim f^{3/2}$ is found from the measurements as well as from the numerical calculations. The larger power values obtained by the fluid modelling of about a factor of 2 in the experimental frequency range can result from differences between the cross-sectional area A_{dis} used in the model in (9) and the real discharge cross section covered in the experiment.

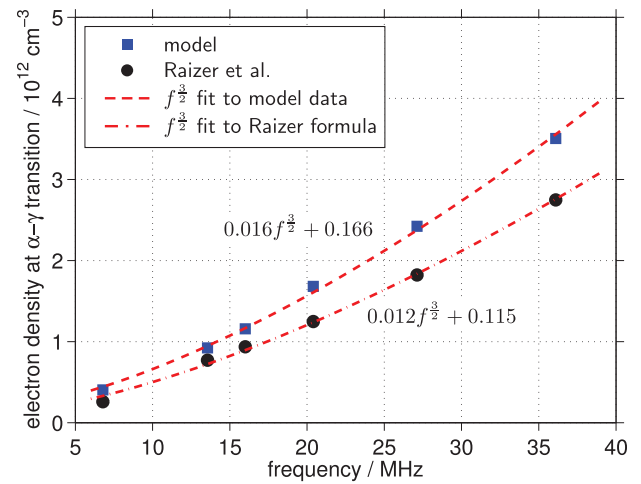


Figure 10. Critical electron density as a function of the applied frequency obtained by fluid modelling and relation (10) according to Raizer *et al* [45].

For further verification and explanation of the observed $f^{3/2}$ scaling for the α - γ transition power, the concept of a critical plasma density n_{crit} for sheath breakdown established by Raizer *et al* [45] for the α - γ transition in moderate pressure RF plasmas is applied. Among others, Yang *et al* [21] and Farouk *et al* [44] have verified that this fundamental theory is applicable at atmospheric pressure RF plasmas, too. According to Raizer *et al* [45], the critical plasma density at which sheath breakdown and consequently a transition from the α to the γ -mode occurs is given by

$$n_{\text{crit}} = \frac{Bp}{(e/\epsilon_0)A' [\ln(A/\ln(1 + \gamma^{-1})) + \ln(2pA')]} \quad (10)$$

where $A = 12 \text{ cm}^{-1} \text{ Torr}^{-1}$ and $B = 180 \text{ V cm}^{-1} \text{ Torr}^{-1}$ are constants in the formula for the ionization coefficient for argon gas [46], $p = 760 \text{ Torr}$ denotes the gas pressure, $\gamma = 0.07$ is the secondary electron emission coefficient used in the model [36], e and ϵ_0 are the elementary charge and the vacuum permittivity, respectively, and A' denotes the oscillation amplitude of the plasma boundary. The latter was determined from the temporal variation of the spatial electron distribution.

In figure 10 the period-averaged electron density at the gap centre obtained by fluid model calculations for the critical α - γ transition power $P_{\text{crit}}(f)$ specified in figure 8 is shown and compared to the theoretical values determined according to formula (10) for different frequencies. Both approaches predict the scaling $n_{\text{crit}} \sim f^{3/2}$ for the critical electron density which is consistent with the observed increase of the α -mode stability range as $f^{3/2}$. The good agreement of the results shown in figure 10 emphasizes the validity of the fluid model.

5.2. Excitation dynamics

Investigations of the spatio-temporal plasma behaviour and its excitation dynamics help to understand the basic processes of the discharge development. Additionally, comparison of measured and calculated data help to validate the results. Therefore, phase resolved measurements of the optical emission and

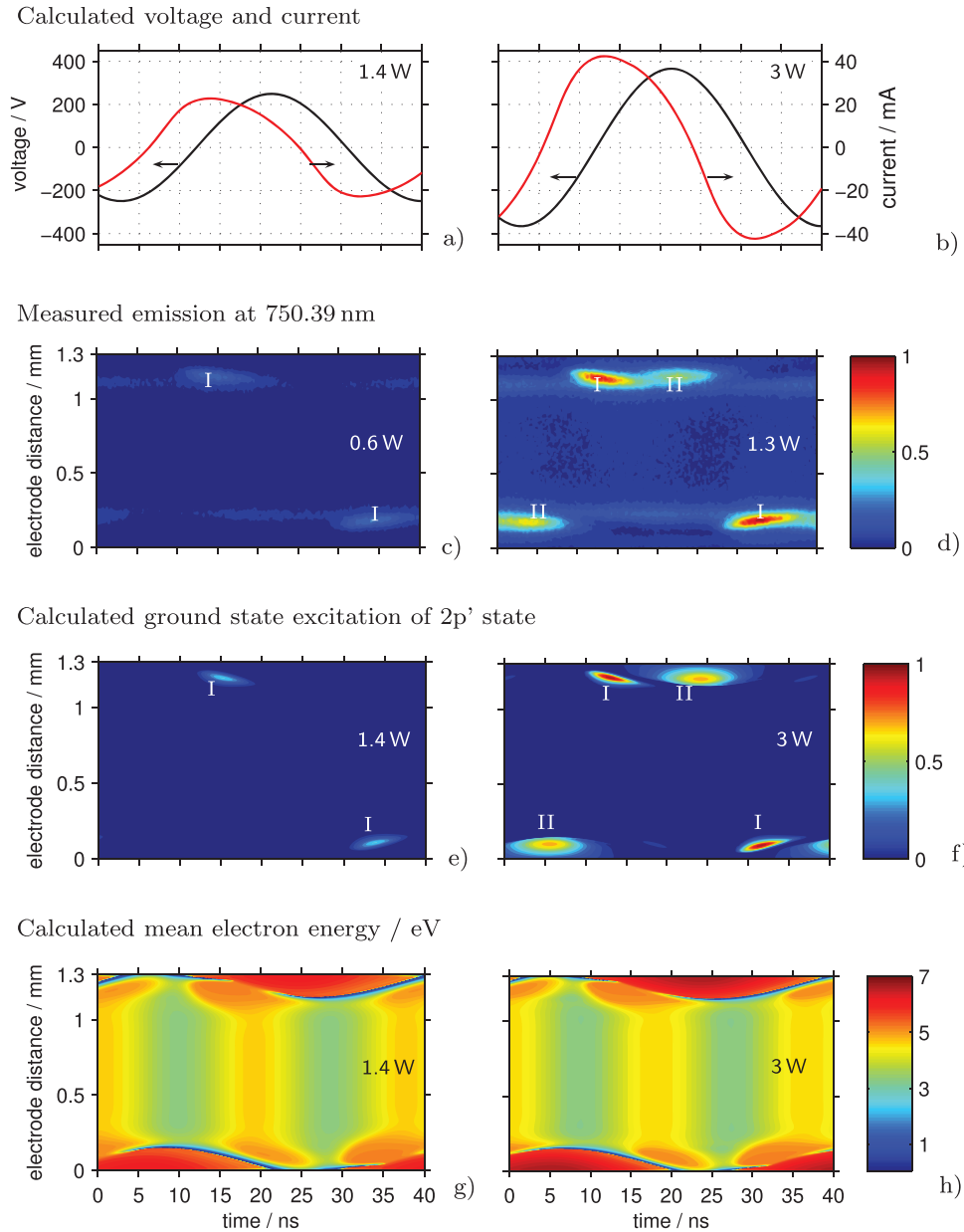


Figure 11. Temporal variation of calculated discharge voltage and current ((a), (b)), measured argon emission at 750.39 nm ((c), (d)), calculated ground state excitation rate of 2p' state ((e), (f)) and calculated mean electron energy ((g), (h)) for two different power settings at 27 MHz. The measured emission and calculated excitation rates are normalized to their respective maximum values at higher power.

time- and space-dependent numerical modelling have been performed for the argon plasma jet running in the α -mode and at the transition to the γ -mode for the frequency of 27 MHz.

Figure 11 represents the measured excitation dynamics of the argon emission at 750.39 nm ($2p_1 \rightarrow 1s_2$ transition, see figure 6) at 0.6 and 1.3 W (figures 11(c) and (d)) together with the numerical results for the discharge voltage and current (figures 11(a) and (b)), the normalized ground state excitation rate of the lumped 2p' state comprising the states $2p_4$ – $2p_1$ (figures 11(e) and (f)) as well as the mean electron energy (figures 11(g) and (h)) at 1.4 and 3.0 W. The respective higher power value in the experiment and for the numerical calculations was chosen as P_{crit} according to figure 9(b) and the lower power values were set well below by the same factor to investigate a representative α -mode discharge.

It is known from the literature that the argon emission at 750.39 nm is mainly caused by direct excitation of ground state atoms according to the reaction $\text{Ar}(1p_0) + e^- \rightarrow \text{Ar}(2p_1) + e^-$, see e.g. [47]. Therefore, the normalized ground state excitation rate of the considered 2p' level is shown in figures 11(e) and (f) for direct comparison with the normalized emission intensity illustrated in figures 11(c) and (d). The PROES measurements of the argon transition at 750.39 nm as well as the calculated excitation rate show one intensity maximum (labelled as I) in every half cycle of the applied voltage for the low power case (α -mode discharge), see figures 11(c) and (e). At the higher power P_{crit} a second maximum (labelled as II) arises immediately after the first one for the experimental and theoretical results as depicted in figures 11(d) and (f). In addition to the very good qualitative reproduction of the excitation

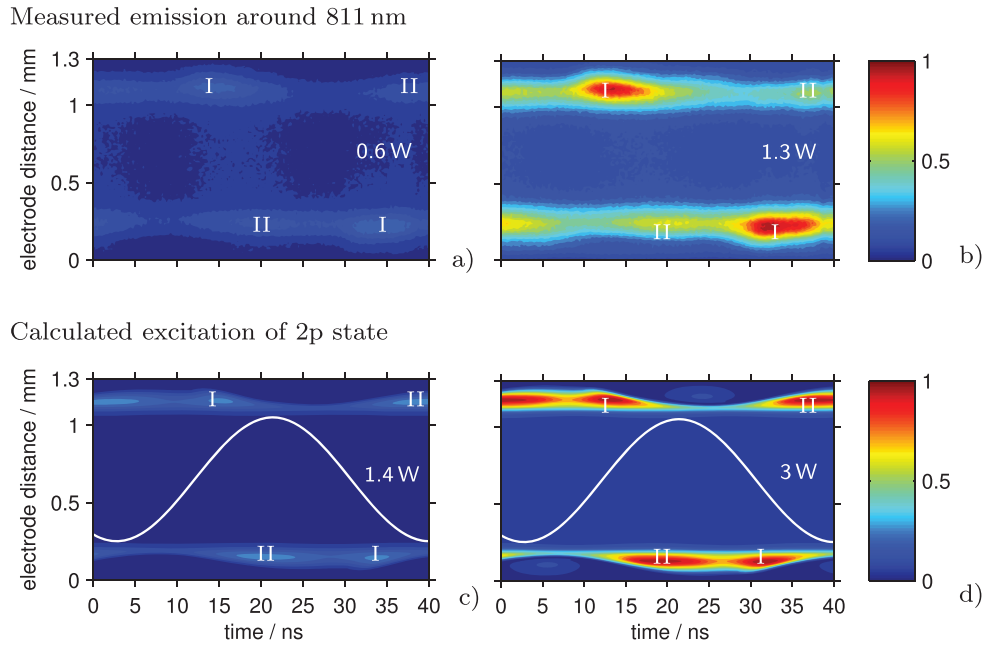


Figure 12. Spatio-temporal variation of the measured argon emission around 811 nm ((a), (b)) and calculated excitation rate of the 2p state ((c), (d)) for two different power settings at 27 MHz. The measured emission and calculated excitation rates are normalized to their respective maximum values at higher power. The white line marks the voltage course for better readability.

dynamics by the fluid model, the numerical results quantitatively describe the measured reduction of the emission intensity of the first maximum (I) at decreased power.

By looking at the temporal variation of the discharge voltage and current in figures 11(a) and (b) it becomes obvious that the first maximum (I) is related in time to the maximum of the current magnitude, whereas the second emission maximum (II) relates to the maximum of the discharge voltage where the electric field in the cathode region is largest. This suggests that secondary processes in the sheath region are responsible for the excitation of the second maximum (II).

In order to clarify the source of the different emission maxima, the spatio-temporal variation of the mean electron energy is represented in figures 11(g) and (h) for the two power cases. It turns out that the advanced drift-diffusion approach [37] used for description of the electron energy transport in the present model provides the possibility to identify clearly the border between bulk electrons and secondary electrons in the plasma sheath. The first maximum (I) arises at the instant where the mean energy of bulk electrons is at its maximum. In contrast, the second maximum (II) can be contributed to the peak of the mean electron energy of secondary electrons accelerated in the sheath due to the strong electric field in front of the instantaneous cathode. This explains why the light emission maxima (I) is always present but the maxima (II) occurs only with transition to the γ -mode in which the mean electron energy in the sheath markedly increases and thus secondary electron emission strongly affects the gas excitation and ionization [16].

In addition to the emission at 750.39 nm, phase resolved measurements of the optical emission around 811 nm ($2p_9 \rightarrow 1s_5$ and $2p_7 \rightarrow 1s_4$ transition, see figure 6) were performed. In figure 12 the measured data for the same power

values as in figure 11 are compared to the according excitation rates of the lumped 2p state included in the model. Unlike the excitation process of the $2p_1$ level, the $2p_9$ level—dominating the emission around 811 nm—is mainly populated by electron impact excitation from metastable levels [47]. Hence, the total excitation rate including ground state excitation as well as stepwise excitation is shown in figures 12(c) and (d) for comparison. Again, it is found that the modelling results mostly match the experimental observations. For both power cases two temporally smeared maxima (labelled as I and II) can be observed in each half-period.

A decrease of the dissipated power leads to the expected intensity drop. This applies for the experimental as well as for the modelling results. In contrast to the emission at 750.39 nm (see figure 11) the general emission pattern remains the same. This difference is caused by the contribution of the stepwise population of the $2p_9$ level that does not contribute to the density of the $\text{Ar}(2p_1)$ atoms. By relating the emission maxima (I) and (II) to the spatio-temporal behaviour of the mean energy of the electrons represented in figures 11(g) and (h) it turns out that the emission pattern around 811 nm displayed in figure 12 is directly connected to the mean energy distribution of the bulk electrons according to the fluid modelling results.

In order to elucidate the role of stepwise excitation processes for the population of the argon 2p level considered in the model, the temporally averaged ground state and stepwise excitation rates predicted by the numerical calculations are shown in figure 13. Obviously, the stepwise excitation exceeds the ground state excitation by more than two orders of magnitude, except for small regions in front of the electrodes where the mean electron energy is largest and the density of excited species is small. This explains why the emission

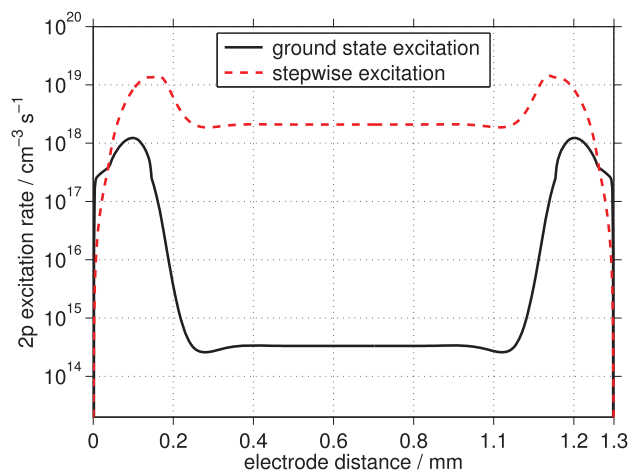


Figure 13. Calculated results of period averaged excitation rates of the lumped 2p level at a power of 3 W and $f = 27$ MHz.

pattern around 811 nm is barely influenced by the changing ground state excitation with changing input power.

6. Conclusion

Experimental and numerical modelling studies have been performed to determine the electrical characteristics and to analyse the stability and excitation dynamics of an argon micro-scaled atmospheric pressure plasma jet. A self-made plasma tuning unit was designed which makes the ignition of discharges in argon within the jet geometry possible. It gives access to a large frequency range and also allows for measurements of the power dissipated in the plasma at selected frequencies. The experimental investigations were complemented by phase resolved optical emission spectroscopic measurements of three selected argon lines. The main features of the electrical and optical measurements were presented, where special focus was placed on the experimental method for the determination of the dissipated power of the plasma. In addition, a time-dependent, spatially one-dimensional fluid model has been applied to analyse the periodic behaviour of the discharge plasma of the argon micro-scaled atmospheric pressure plasma jet, where generally good agreement with the measured properties was obtained.

The experimental investigations of discharges in the α -mode up to the transition to the γ -mode for different frequencies showed that the RMS voltage and the dissipated power at the α - γ transition exhibit a dependence on the applied frequency f according to f^{-1} and $f^{3/2}$, respectively. These functional dependences coincide well with the fluid modelling results obtained for a larger frequency range. The analysis of these results has led to a scaling law of the α - γ transition power with $f^{3/2}$ which is also in agreement with the established concept of a critical plasma density for sheath breakdown.

Regarding the excitation dynamics of the different excited argon states investigated at the frequency of the jet of 27 MHz, it was found that the emission structure at 750.39 nm coming from the energetically higher state Ar(2p₁) is more sensitive to a variation of the applied power and of different origin than that around 811 nm resulting mainly from Ar(2p₀). The latter

emission pattern remains almost the same in the power range considered and is significantly affected by stepwise excitation processes according to the fluid modelling results. In contrast, a second maximum in the excitation structure of the 750.39 nm emission at the α - γ transition point occurs at each half cycle of the applied voltage as a result of the impact of secondary electrons emitted from the electrodes in addition to a first maximum observable already at lower power caused by direct excitation of ground state atoms.

The studies of the micro-scaled atmospheric pressure plasma jet clearly demonstrate that this jet, usually run with helium as the feed gas, can be operated well in argon for different applied frequencies at defined operation conditions and that the main features of its periodic behaviour are understandable on the basis of electrical and optical measurements in combination with numerical modelling, proving a scaling law of the α - γ transition power with $f^{3/2}$.

Acknowledgments

This work was partly funded by the German Ministry of Education and Research (BMBF, grant 03Z2DN12) and was additionally supported by the German Research Foundation within the Transregional Collaborative Research Centre Transregio 24 ‘Fundamentals of complex plasmas’ and under grant LO 623/3-1. P Lüttjohann is acknowledged by SI for his assistance with the power measurements. SR thanks V Schulz-von der Gathen for various discussions about the μ APPJ and the reference jet.

References

- [1] Lu X, Laroussi M and Puech V 2012 *Plasma Sources Sci. Technol.* **21** 034005
- [2] von Woedtke T, Reuter S, Masur K and Weltmann K D 2013 *Phys. Rep.* **530** 291–320
- [3] Niemi K, Reuter S, Schaper L, Knake N, Schulz-von der Gathen V and Gans T 2007 *J. Phys.: Conf. Ser.* **71** 012012
- [4] Schulz-von der Gathen V, Schaper L, Knake N, Reuter S, Niemi K, Gans T and Winter J 2008 *J. Phys. D: Appl. Phys.* **41** 194004
- [5] Niemi K, Reuter S, Graham L M, Waskoenig J and Gans T 2009 *Appl. Phys. Lett.* **95** 151504
- [6] Reuter S 2008 *Formation Mechanisms of Atomic Oxygen in an Atmospheric Pressure Plasma Jet Characterised by Spectroscopic Methods* (Göttingen: Cuvillier)
- [7] Waskoenig J, Niemi K, Knake N, Graham L M, Reuter S, Schulz-von der Gathen V and Gans T 2010 *Pure Appl. Chem.* **82** 1209–22
- [8] Hemke T, Wollny A, Gebhardt M, Brinkmann R P and Mussenbrock T 2011 *J. Phys. D: Appl. Phys.* **44** 285206
- [9] Schulz-von der Gathen V, Buck V, Gans T, Knake N, Niemi K, Reuter S, Schaper L and Winter J 2007 *Contrib. Plasma Phys.* **47** 510–9
- [10] Schaper L, Reuter S, Waskoenig J, Niemi K, Schulz-von der Gathen V and Gans T 2009 *J. Phys.: Conf. Ser.* **162** 012013
- [11] Schneider S, Dünbnier M, Hübner S, Reuter S and Benedikt J 2014 *J. Phys. D: Appl. Phys.* **47** 505203
- [12] Knake N, Reuter S, Niemi K, Schulz-von der Gathen V and Winter J 2008 *J. Phys. D: Appl. Phys.* **41** 194006

- [13] Niermann B, Böke M, Sadeghi N and Winter J 2010 *Eur. Phys. J. D* **60** 489–95
- [14] O’Connell D, Cox L J, Hyland W B, McMahon S J, Reuter S, Graham W G, Gans T and Currell F J 2011 *Appl. Phys. Lett.* **98** 043701
- [15] Marinov D and Braithwaite N S J 2014 *Plasma Sources Sci. Technol.* **23** 062005
- [16] Shi J J and Kong M G 2005 *J. Appl. Phys.* **97** 023306
- [17] Moon S Y, Rhee J K, Kim D B and Choe W 2006 *Phys. Plasmas* **13** 033502
- [18] Shi J J and Kong M G 2007 *Appl. Phys. Lett.* **90** 101502
- [19] Chirokov A, Khot S N, Gangoli S P, Fridman A, Henderson P, Gutsol A F and Dolgopolsky A 2009 *Plasma Sources Sci. Technol.* **18** 025025
- [20] Vidaud P, Durrani S M A and Hall D R 1988 *J. Phys. D: Appl. Phys.* **21** 57
- [21] Yang X, Moravej M, Nowling G R, Babayan S E, Panelon J, Chang J P and Hicks R F 2005 *Plasma Sources Sci. Technol.* **14** 314–20
- [22] Park J, Henins I, Herrmann H W, Selwyn G S and Hicks R F 2001 *J. Appl. Phys.* **89** 20–8
- [23] Shi J J and Kong M G 2005 *Appl. Phys. Lett.* **87** 201501
- [24] Walsh J L, Iza F and Kong M G 2008 *Appl. Phys. Lett.* **93** 251502
- [25] Liu D W, Iza F and Kong M G 2009 *Plasma Process. Polym.* **6** 446–50
- [26] Zhang J, Ding K, Wei K, Zhang J and Shi J 2009 *Phys. Plasmas* **16** 090702
- [27] Qian Y J, Ding K, Song S T, Guo Y, Zhang J and Shi J J 2012 *Contrib. Plasma Phys.* **52** 289–94
- [28] Ding K, Lieberman M A, Lichtenberg A J, Shi J J and Zhang J 2014 *Plasma Sources Sci. Technol.* **23** 065048
- [29] Park J, Henins I, Herrmann H W and Selwyn G S 2001 *J. Appl. Phys.* **89** 15–9
- [30] Hofmann S, van Gessel A F H, Verreycken T and Bruggeman P 2011 *Plasma Sources Sci. Technol.* **20** 065010
- [31] Puac N, Petrovic Z L, Malovic G, Dordevic A, Zivkovic S, Giba Z and Grubisic D 2006 *J. Phys. D: Appl. Phys.* **39** 3514–9
- [32] Godyak V and Piejak R 1990 *J. Vac. Sci. Technol. A* **8** 3833–7
- [33] de Rosny G, Mosburg E R, Abelson J R, Devaud G and Kerns R C 1983 *J. Appl. Phys.* **54** 2272–5
- [34] Schulze J, Schüngel E, Donkó Z, Luggenhölscher D and Czarnetzki U 2010 *J. Phys. D: Appl. Phys.* **43** 124016
- [35] Crintea D L, Czarnetzki U, Iordanova S, Koleva I and Luggenhölscher D 2009 *J. Phys. D: Appl. Phys.* **42** 045208
- [36] Becker M M, Hoder T, Brandenburg R and Loffhagen D 2013 *J. Phys. D: Appl. Phys.* **46** 355203
- [37] Becker M M and Loffhagen D 2013 *AIP Adv.* **3** 012108
- [38] Becker M M and Loffhagen D 2013 *Adv. Pure Math.* **3** 343–52
- [39] Leyh H, Loffhagen D and Winkler R 1998 *Comput. Phys. Commun.* **113** 33–48
- [40] Hagelaar G J M and Pitchford L C 2005 *Plasma Sources Sci. Technol.* **14** 722–33
- [41] Grubert G K, Becker M M and Loffhagen D 2009 *Phys. Rev. E* **80** 036405
- [42] Pipa A V, Ionikh Y Z, Chekichev V M, Dünnebier M and Reuter S 2015 *Appl. Phys. Lett.* **106** 244104
- [43] Niemi K, Reuter S, Graham L M, Waskoenig J, Knake N, Schulz-von der Gathen V and Gans T 2010 *J. Phys. D: Appl. Phys.* **43** 124006
- [44] Farouk T, Farouk B, Gutsol A and Fridman A 2008 *Plasma Sources Sci. Technol.* **17** 035015
- [45] Raizer Y P, Shneider M N and Yatsenko N A 1995 *Radio-Frequency Capacitive Discharges* (Boca Raton, FL: CRC)
- [46] Raizer Y P 1991 *Gas Discharge Physics* (Berlin: Springer)
- [47] Boffard J B, Lin C C and DeJoseph C A Jr 2004 *J. Phys. D: Appl. Phys.* **37** R143